Slip distributions on active normal faults measured from LiDAR and field mapping of geomorphic offsets: an example from L'Aquila, Italy, and implications for modelling seismic moment release.

Wilkinson, Max[1]; Roberts, Gerald P. [2]; McCaffrey, Ken[1]; Cowie, Patience A.[3]; Faure Walker, Joanna P. [4], Papanikolaou, Ioannis[5], Phillips, Richard J. [6]; Michetti, Alessandro[7]; Vittori, Eutizio[8].

[1] Department of Earth Sciences, South Road, Durham University, Durham, UK DH1 3LE
[2] Department of Earth and Planetary Sciences, Birkbeck, University of London, London, UK WC1E 7HX
[3] University of Bergen, Department of Earth Science, P.O.Box 7803, N-5020 Bergen, Norway
[4] Institute of Risk and Disaster Reduction, UCL, University of London, UK WC1E 7HX
[5]Laboratory Mineralogy – Geology, Agricultural University of Athens
[6]Institute of Geophysics and Tectonics, University of Leeds, Leeds, UK LS2 9JT
[7]Dipartmento Di Scienze Chimiche E Ambientale, Via Valleggio 11, 22100, Como, Italy
[8]Servizio Geologico d'Italia, ISPRA, Via Curtatone, 3 – 00185 Roma

Abstract

Surface slip distributions for an active normal fault in Italy have been measured using terrestrial laser scanning (TLS), concentrating on offsets developed since 15 ±3 ka and for 2 palaeoearthquake ruptures, in order to assess the impact of spatial changes in fault orientation and kinematics on sub-surface slip distributions that control seismic moment release. The southeastern half of the surface trace of the Campo Felice active normal fault near the city of L'Aquila, central Italy, was scanned with TLS to define the vertical and horizontal offsets of geomorphic slopes that formed during the last glacial maximum (15 ±3 ka) from the centre of the fault to its southeastern tip. Field measurements were made to define the strike and dip of the fault plane and plunge and plunge direction of the slip vector from striations on slickensides. Fault kinematics from 43 sites and throw/heave measurements from 250 scarp profiles were analysed using a modification of the Kostrov equations to calculate the magnitude and directions of the horizontal principle strain-rates. The studied 5 km long portion of the fault has an overall strike of 140^{o}, but has a prominent bend where the strike is 100-140^{o}, where the fault has linked across a former left-stepping relay-zone which had an along strike length of ~600 m and across strike width of ~300 m. Throw-rates defined by TLS profiles across a 15 ±3 ka bedrock fault scarp decrease linearly from 0.95 ±0.025 mm/yr at the fault centre through 0.5 ±0.025 mm/yr to zero at the fault tip, except in the position of the prominent bend where throws rates increase by 0.15 ±0.025 mm/yr over a distance of ~1 km. The vertical coseismic offsets averaged between two palaeoearthquake ruptures that manifest themselves as fresh stripes of rock at the base of the bedrock scarp, also increase across the

prominent bend from 0.66 ±0.05 m to 1 ±0.05 m. Both the dip of the fault (~50°), and slip-vector azimuth (205-218°) are constant across the prominent bend. These combine to produce a principle strain-rate calculated in 250 x 250 m boxes centred on the fault trace that decreases linearly from ~3.5 ppm/yr to ~1 ppm/yr from the fault centre towards its tip; the strain-rate does not increase across the prominent fault bend. The above shows that changes in fault strike, whilst having no effect on the principle horizontal strain-rate, can produce local maxima in throw-rates of ~25%, and these throw-rate maxima can also be seen in slip distributions for palaeoearthquakes. We discuss the implications of the above for modelling sub-surface slip distributions for earthquake ruptures through inversion of GPS, InSAR and strong motion data using planar fault approximations, referring to recent examples on the nearby Paganica fault that ruptured in the Mw 6.3 2009 L'Aquila Earthquake, where slip anomalies of 20-30% of the total slip are considered significant, yet small-scale changes in fault orientation are not modelled.

Introduction

The spatial distribution of geomorphic offsets across active normal faults reveal that surface fault traces are not linear features, but instead are characterised by discontinuities such as relay zones and bends in the fault trace (Faure Walker et al. 2009). It is well-known that surface ruptures to earthquakes follow these discontinuities, wrapping around bends in the fault trace or crossing relay zones (Roberts 1996), implying that at depth the fault is continuous across such surface discontinuities. The surface slip distribution can be examined by geomorphologists, in contrast to the sub-surface slip distribution. The subsurface slip distribution is important because (1) it defines the ruptured area and amount of slip, which alongside the stiffness of the deforming material define the seismic moment, or energy release in an earthquake (Kostrov 1974, Wells and Coppersmith 1994), and (2) is used to calculate how stress has been transferred onto fault surfaces that were not ruptured in that particular earthquake, but could represent the sites of future earthquake rupture (e.g. Walters et al. 2009). In this paper we show that although the sub-surface slip-distribution is beyond the direct observation of geomorphologists, geomorphic observations of the surface slip distribution can provide important constraints on these earthquake processes. In particular, Faure Walker et al. (2009) showed that offsets of dated geomorphic surfaces across fault scarps, combined with measurements of the strike and dip of the fault plane and plunge and plunge direction of the slip vector, can be used to derive the relationship between (i) the vertical and horizontal motions of the rocks around the fault, (ii) the amount of slip on the fault plane itself, and (iii) strain-rates implied by such motions, and how these relate to regional strain-rates imposed by motions between and within tectonic plates. In order to maintain the imposed strain-rate at locations where small scale bends in the strike of normal faults exist, Faure Walker et al. (2009) showed that the rate of throw accumulation must increase relative to the rest of the fault, because vertical and horizontal motions, slip on the fault and strain rates are inter-related (see Method Section).

Despite this, sub-surface slip distributions for normal faulting earthquakes are commonly modelled assuming planar fault geometries with no bends in the fault trace, contrary to data from the fault-related geomorphology. For example, a number of authors have attempted to invert data from GPS and InSAR collected over a time period encompassing the Mw 6.3 2009 L'Aquila Earthquake in Italy (Fig. 1). The vertical and horizontal motions recorded geodetically across the Paganica Fault ruptured in 2009 have been used to iteratively-model the sub-surface slip, utilising elastic half-space dislocation models. Modelling is facilitated by assumptions concerning the shear modulus, Poisson's ratio and rheological layering, and, in general, a planar fault is assumed and discretised into relatively small (~1 x 1 km) patches on a larger fault surface (~25 x 15 km). The vertical and horizontal motions are used to retrieve the slip on the idealised fault plane. We note a variety of solutions from different authors for this type of modelling (Fig. 1), but note that in what is probably the most sophisticated attempt at this modelling by D'Agostino et al. (2012), the maxima in sub-surface coseismic slip underlies the area where greatest coseismic subsidence was measured at the surface with InSAR. This asymmetry, where the maximum modelled slip is skewed towards the SE end of the fault is present in the slip distributions of D'Agostino et al. (2012), Atzori et al. (2009), Cirella et al. (2009), Cheloni et al. (2010) and Walters et al. (2009), consistent with the observation that maximum surface subsidence recorded by InSAR is skewed in the same way (compare Fig. 1a with 1b-e). Crucially for this paper, we also note that the slip maxima lies down-dip of a 1-2 km across-strike relay-zone (labelled R in Fig. 1a) between two of the fault traces that ruptured during the earthquake. Here we ask the question as to what the relationship is between this relay-zone (non-planarity of the fault plane), slip on the fault plane at depth and vertical motions of the ground surface recorded by InSAR and GPS. We suspect following Faure Walker et al. (2009), that the relay zone may overlie a zone of non-planarity in the fault plane at depth that may have induced anomalous surface deformation. Calderoni et al (2012) have suggested from an analysis of fault-trapped seismic waves that the fault segments at surface are part of a continuous fault system at depth. Unfortunately, the Paganica Fault is poorly-exposed relative to other nearby faults and thus the geomorphic signature of slip and fault kinematics are difficult to retrieve for this fault, so we have been unable to directly apply the theory from Faure Walker et al. (2009). Thus, to ask the above question, and quantify how much the vertical deformation is affected by bends in fault traces, we utilise observations of a well-exposed fault located ~15 km to the SSW of the faults ruptured in 2009 - the Campo Felice active normal fault. The Campo Felice fault exhibits a well-exposed bedrock fault scarp that records slip since the last-glacial maximum (15 ±3 kyrs), and has clear evidence of coseismic slip in past earthquakes in the form of stripes of freshly-exposed rock at the base of the fault plane. The relationship between vertical motions, slip on the fault and strain-rate can be retrieved across a prominent bend in the strike of the fault trace because the fault plane is well-preserved and exhibits numerous examples of slickenside surfaces covered in frictional-wear striae that record the slip vector orientation. We have measured the orientations of the fault plane and slip-vector in the field, and scanned the geomorphology of the site using terrestrial laser-scanning (TLS) to retrieve the amounts of slip on the fault and the vertical motion recorded by offset geomorphology in 3D. We use this information on the Campo Felice fault to discuss the likely patterns of slip at depth on the neighbouring Paganica Fault.

Geological background

The central Apennines contains active normal faults, such as the Campo Felice, Parasano and Paganica faults discussed in this paper (Fig. 2; Galadini and Galli 2000, Roberts and Michetti 2004, Pace et al. 2006, Faure Walker et al. 2010). Extension during the Plio-Pleistocene has been located on the high topography of the Apennine mountains, the site of an older, submarine foreland thrust belt produced during Cretaceous-Miocene Alpine convergence. The normal faults offset pre-rift Mesozoic and Tertiary carbonates and have produced localised inter-montane basins in their hangingwalls. The extension is associated with uplift and formation of the topography of the Apennines mountains (D'Agostino et al. 2001, Faure Walker et al. 2012).

Active normal faulting in the central Apennines is associated with a long recorded history and palaeoseismic record of past earthquakes (Galli et al. 2008). Events like the 1915 Mw 6.9-7.0 Fucino earthquake (33,000 deaths) and the 2009 Mw 6.3 L'Aquila earthquake (309 deaths) have ruptured faults that are now well-mapped with clear surface faulting (Michetti et al. 1996, Boncio et al. 2009). The L'Aquila earthquake ruptured the Paganica Fault with surface vertical offsets of 10-15 cm through the town of Paganica, with continuation of the mapped ruptures both northwest and southeast of the town. Observations with InSAR and GPS demonstrate coseismic subsidence of up to 25 cm between 5-6 km into the hangingwall of the fault (Fig. 1 a; see D' Agostino et al. 2012 for a review). Elastic dislocation modelling suggests this implies over 80 cm of slip at depth on the fault (Fig. 1b-f; Papanikolaou et al. 2010, D' Agostino et al. 2012 for a review). This area with high values of surface subsidence, and implied area of high slip at depth, is skewed in location towards the southeastern end of the surface ruptures. Unfortunately, the surface ruptures occur in unconsolidated slope sediments in most places, so the orientation of the fault plane and the slip vectors of the earthquake are relatively poorly constrained, except in the central portion of the rupture within the town of Paganica where a study of offset tarmac and concrete surfaces along the rupture revealed the slip vector plunges at 21^{o} towards 218^{o} (±5^{o}), almost perpendicular to the strike of the fault (127^{o}), at least at the surface (Roberts et al. 2010). The relatively poor exposure of the ruptures to the 2009 earthquake led us to study the kinematics of neighbouring active normal faults. Below we report a study of the nearby Campo Felice fault accomplished using terrestrial laser scanning (TLS) and field structural mapping and analysis.

Method

A TLS point cloud dataset of the Campo Felice fault was acquired using a Riegl LMS-z420i laser scanner. The dataset consisted of six scan positions and 11 million points, covering the entire 5 km length of the Campo Felice fault (Fig. 4a). The point clouds from each scan position were co-registered using the RiSCAN pro processing software. This process correctly unites the point clouds from each scan position within 3D space. Geo-referencing was carried out by surveying a network of cylindrical reflectors present within each point cloud using real time kinematic (RTK) GPS. The UTM 33T co-ordinate system with WGS84 datum was chosen. The vertical offsets that define the surface slip distribution can be recovered from these data, but first a number of data processing steps are required.

A terrestrial laser scanner acquires a point cloud dataset by using the time of flight of sequentially emitted and reflected laser pulses to calculate the range between the laser scanner and objects within its line of sight. By incrementally adjusting the emission direction in horizontal and vertical steps, the scanner is able to sample reflections on a regularly spaced grid within the line of sight of the scanner. For each laser return a unique point in 3D space is calculated, with individual returns populating a point cloud dataset (Fig. 4a). Laser returns can occur from the ground surface, bare rock, vegetation or other similar objects such as fence posts and buildings.

The first step in processing the point cloud is to remove all points that do not represent ground returns. This step can be carried out manually in the case of small study areas with limited vegetation by selecting and deleting vegetation from within a 3D viewer, such as in the processing software RiSCAN pro. This process can preserve most of the ground points, with little degradation, although it can be unrealistically time consuming in the case of larger study areas. A sensible compromise is to remove the most easily identifiable patches of vegetation and lone trees manually before applying a vegetation filter or algorithm to the point cloud. In this study, a pseudo-vegetation filter was applied to the point cloud using the GEON *points2grid* software [Crosby et al., in review]. *Points2grid* was developed to create raster elevation grids from point cloud data. The software operates by allowing the user to define an output grid spacing *S*, which will determine the uniform point spacing in map view of the output pointset. The software also requires a search radius to be defined, and for the case of the pseudo-vegetation filter, the minimum elevation option selected. *Points2grid* in this case calculates the elevation value for each output point according to the minimum elevation found in the input pointset within the specified search radius *R* (Fig. 4 b and c). As a general rule, the search radius should be:

$$R = \frac{\sqrt{2}}{2} * S$$

The effect is that the points with vegetation have higher elevation values than the ground surface and are removed from the output pointset. A side effect of the process is that the input point cloud is also decimated and re-sampled as a regularly spaced pointset. This can be beneficial, as the fewer points that are used to represent the topography the more options are available for intensive post-processing to create derivatives for use in analysis. It is important however not to over-filter the data as this can lead to over-simplification of the output pointset and the removal of the important topographic features which exist beneath the vegetation. As a general rule, an output point spacing of between 2 – 4 meters, with corresponding search radius R between 1.41 – 2.8 meters seems to be most suitable for the TLS datasets from the active normal fault collected during this study. It is most suitable because it preserves metres-scale changes in the actual topography while still being large enough to eradicate vegetation. Once the point cloud has been filtered to remove vegetation there are a number of derivatives that can be created from the dataset in order to identify geomorphic features.

The generation of a solid surface from a point cloud dataset allows a more complete appreciation of the topographic point cloud dataset. A solid surface representation of the topography is created using the vegetation-filtered pointset as input. The simplest way to create a representative surface from a pointset is by the creation of a triangular irregular network (TIN). A TIN is a triangulated mesh, whereby the vertices of each triangle are located using the input pointset. It is essentially a method of joining the points together and filling the internal space between three points with a plane. The most common method of choosing groups of three points to form triangles is through Delaunay triangulation [Delaunay, 1934], whereby all points are used as triangle vertices, such that no triangles can be subdivided using points located within a triangle and that the smallest angle of each triangle is the largest from the possible combinations. The process favours triangulation options that produce equilateral triangles and those with very large differences between the lengths of their sides are avoided. A major advantage of surface generation by TIN using Delaunay triangulation over more complex routines is that the process is computationally efficient. The point cloud processing software RiSCAN pro is able to generate TIN surfaces from point cloud datasets using Delaunay triangulation (Fig. 4d). The generation of a TIN surface, with lighting applied from a unidirectional source allows immediate identification of the base of the fault scarp, footwall gullies and hangingwall erosional channels (Fig 4d and e).

A further enhancement to a TIN surface is to calculate the dip of each triangle from horizontal using the dip calculation algorithm in the program goCAD, and then to interpolate this data over the entire surface. This interpolated data can then be used to colour the surface according to the local dip, using a colour map, creating a surface dip map as shown in Figure 4e. Surface dip (slope) maps allow a quantitative assessment of the surface to be carried out. Geomorphic features such as bowl shaped rotational slips and alluvial fans are clearly defined using this technique, as opposed to viewing the surface without a dip colourmap applied. The creation of a surface slope map also allows for the dip of the fault scarp, hangingwall and the footwall to be visualised in their entirety.

The generation of topographic contours (lines connecting points of equal elevation) allow a further method of surface assessment. Topographic contours were generated in goCAD using the contour algorithm from within the surface attributes toolbox and are displayed directly on the surface. Topographic contours provide a means with which to measure the uniformity of a slope, for example the hangingwall of an active normal fault. Contours in a particular region of the hangingwall that are linear and equally spaced signify that this region of the hangingwall has not been modified by the geomorphic processes that could affect the measured fault slip. On the other hand topographic contours that are curved and non-equally spaced signify geomorphic features such as rotational slips, alluvial fans and erosional channels and footwall bedrock gullies (e.g. Fig. 4g).

Geomorphic processes alter the perceived surface offset along active faults and are an important consideration for earthquake geologists. In order to study surface offsets produced solely by fault slip during earthquakes it is necessary to select study sites within the TLS dataset which have not had their surface offset altered by geomorphic processes such as erosional gullying, colluvial and alluvial fan sedimentation or landslides. Attribute map, examples of which are given in Figures 4d-g, were used to identify sites where exhumation of the fault scarp and fault plane were solely through fault slip and unaffected by mass movement, erosion or sedimentation; we found twenty five such study sites that are free from the effects of such geomorphic processes. Topographic cross sections were created at each of these sites from the surface TIN using the cross section (surface profile) tool in RiSCAN pro. At each site ten topographic cross sections were created in parallel, spaced at 1 m intervals (Fig. 4e), producing two hundred and fifty in total. Each of the topographic cross sections (e.g. Fig. 5) were interactively interpreted for throw using the program *Crossint* written by the first author in the GNU octave language.

To utilise *Crossint*, a vertically dipping plane was created in RiSCAN pro, which was rotated and translated so that it intersected the TIN in a correct location and trend to create a topographic cross section close to perpendicular to the strike of the fault. The location of the topographic cross section to be generated was checked against the mapped geomorphology to ensure the site was suitable. A batch of ten topographic cross sections, spaced 1 m apart are created using the cross section tool in RiSCAN pro. The tool uses the intersection of the TIN and the vertically dipping plane to create the first cross section, the next cross section is then created at a spacing of 1 m from the first, in the direction of the normal to the plane. The process continues until ten cross sections have been created. The vertically dipping plane is then translated along the fault scarp to the next suitable site for cross section generation, the plane is rotated perpendicular to strike, the geomorphology of the site is checked and the next set of cross sections are generated. The process was repeated until cross sections were generated for all suitable sites along the fault.

The generated topographic cross sections were exported from RiSCAN pro in drawing exchange format (.dxf) and imported into goCAD, which was used to convert the .dxf format files to space delimited ascii text in the form x y z. From this point each of the topographic cross section files are interpreted using *Crossint*. The program is loaded from within the GNU octave terminal and prompts the user to enter the name of the cross section to be interpreted. The user enters the name of the first ascii x y z cross section file to process the first cross section. The x y z data from the cross section file is read by the program, and displayed as a cross sectional plot (Fig. 5). The user then picks two points in the hangingwall using the mouse, between which they are happy a representative portion of the hangingwall exists. *Crossint* then produces a linear regression through all cross section points which exist between the selected points, plots a best fit line and reports the inclination of the line (Fig. 5c and d). the user then confirms interpretation of the hangingwall surface. The user is then prompted to pick two points on the scarp. Once the user has picked these two points, *Crossint* repeats the linear regression for the picked section of the scarp, plots the best fit line and reports the dip of the line (Fig. 5c and d), the user confirms the regression line as a representation of the scarp. The user then picks two points in the footwall, between which an appropriate representation of the footwall exists. *Crossint* repeats the regression for those points and plots the best fit line. The intersection of the hangingwall regression line and the scarp regression line is given as the lower point of the scarp. The intersection of the scarp regression line and the footwall regression line is given as the upper point of the scarp. The throw and heave displayed on the interpreted cross section are the vertical and horizontal differences between these two intersection points. *Crossint* displays the throw and heave for the present interpretation, based on the picked points; the user confirms the interpretation, or has the option to start over. The accepted interpretation, with the picked points and the regression lines is output to a scalable vector graphics file (.svg), along with annotation detailing the inclination of the regression lines and the calculated throw and heave (Fig. 5). This process was repeated for all 250 cross sections from the Campo Felice fault.

Field measurements were collected along the entire length of the Campo Felice fault. The collected measurements comprised the strike and dip of the exposed fault scarp surface, and the slip direction measured from the plunge direction of fault striae (Fig. 6). The field measurements were taken using a compass clinometer with locations provided by real time kinematic GPS with centimetre precision. In order to visualise the changing geometry and slip direction of the fault along its length, the GPS locations were converted to distance along the fault, from the North-Western end, to be plotted on the x-axis against the various measurements from the TLS analysis.

A strain-rate profile (Fig. 7) was calculated from data of throw, fault geometry and kinematic slip, using the method described by Faure Walker et al. (2009) (Table 1). The advantage of converting to strain-rate instead of throw-rate is that strain-rate is independent of variations in fault geometry and of the direction of kinematic slip, as suggested by Faure Walker et al. (2009). Strain-rate is calculated for boxed shaped areas using the equations below, as defined by Faure Walker, et al. (2009). The components of strain e_{11}, e_{12} and e_{22} are calculated for each sample box of width L and area a. T represents the average throw measured on the fault within the sample box and t is the time period over which that throw has formed (for instance 15 ±3 kyrs in the case of post glacial faulting in the central Apennines). The average values of kinematic plunge direction (*plungedir*), kinematic slip direction (*slipdir*) and strike (*strike*) for field measurements within the sample box are also used. The direction of principal strain for each box is then defined by θ. The strain-rate for each box (*strainrate*) is then calculated in the direction of the regional principal strain direction, defined by the average of the values of θ for each sample box along the fault.

$$e_{11} = \frac{1}{at} LT \cot(plunge)\sin(slipdir)\cos(strike)$$

$$e_{22} = \frac{-1}{at} LT \cot(plunge)\cos(slipdir)\sin(strike)$$

$$e_{12} = \frac{1}{2at} LT \cot(plunge)\cos(slipdir + strike)$$

$$\theta = \frac{\arctan(2\frac{e_{12}}{e_{11} - e_{22}})}{2}$$

$$strainrate = \frac{e_{11} + e_{22}}{2} - \frac{e_{11} - e_{22}}{2}\cos(2\theta_{ave}) - e_{12}\sin(2\theta_{ave})$$

Results

Figure 7 shows how the strike, dip, kinematics, throw-rate, strain-rate and coseismic slip for palaeoearthquakes vary along the studied portion of the Campo Felice fault. The measurements for fault strike (Fig. 7a) describe two linear segments, located between 0 – 1500 m and 3000 – 4750 m distance along the fault. The two linear segments have strikes of ~126° ±10 and ~148° ±20 respectively. The section of the fault at 1500 – 3000 m, between these two segments has a strike which describes a curved geometry from ~126° at 1500 m, to a low of 100° ±10 at 2175 m, increasing to ~140° at 3000 m. The field measurements of fault dip (Fig. 7b) show fault dip to be consistent along the length of the fault, with little change in fault dip outside of the measurement precision of ±3°. The mean fault dip is 54° (±1σ = 3.1), the minimum and maximum measured dips are 48° and 61° respectively. The field measurements for the direction of slip (Fig. 7c), collected from kinematic fault striae are consistent between 0 – 3000 m distance along the fault, with a mean slip direction of 211° ($\pm 1\sigma = 3.9$). The slip direction becomes increasing oblique towards the South-Eastern tip, in the direction of the centre of the fault. The direction of slip increases from ~211° at 3000 m distance along the fault to ~250° at the tip at 4750 m distance along the fault.

Data analysis of the interpretation of twenty five cross section locations (250 individual scarp profiles) produced a profile of throw post 15 ± 3 ka for the studied portion of the Campo Felice fault (Fig. 7d) The throw profile shows 1σ precisions for measurement of throw only, calculated from the mean and hence standard deviation of throw interpreted from the ten individual scarp profiles that have been combined for each location, reinforcing the advantages of using LiDAR and *Crossint*. The profile describes a gradual increase in post 15 ± 3 ka throw along strike from zero at the fault tip, through a value of ~7 m where the fault scarp begins to have a clear geomorphic expression to ~14 m at the North-Western end of the studied portion of the fault. We estimate that, given good exposure, it would be possible to identify scarps with throws as small as 1-2 metres. However, the exposure close to the southwestern fault tip are degraded by mass-wasting and in this instance we have not been able to measure right up to the fault tip.

Superimposed on this general increase in post 15 ± 3 ka throw from South-East to North-West is a local increase between 1500 – 3500 m distance along the fault (Fig. 7d). The local increase reaches a maximum of ~11 m at ~2400 m distance along the fault, representing a 17% increase from the value of ~9.5 m depicted at the local minimum at ~1600 m distance.

For comparison with, and calculation of strain-rates, we also show the post 15 ± 3 ka throw data discretised into 250 m sections of the faults (Fig. 7e red line). Strain-rates were calculated using data from Fig. 7a-e. The strain-rate profile (Fig. 7e green line), is calculated from data of throw, fault geometry and kinematic slip, using the method described by Faure Walker et al. (2009). The strain-rate profile differs from the throw-rate profile in that irregularities in throw are not replicated in the strain-rate profile. Strain decreases in an almost linear fashion from a maximum of ~3.51 ppm/yr at the North-Western exposed end of the Campo Felice fault to ~1.04 ppm/yr close to the tip at the South-Eastern end of the fault.

In addition we have examined the vertical offsets produced by what appear to be at least two palaeoearthquakes along the portion of the fault we have studied (Fig. 7f and g). Giaccio et al. (2002) identified colour banding at the base of the exposed fault planes with stripes defining vertical offsets as large as 1.2 m, and, through analogy with colour bands that are known to have been produced elsewhere by earthquake surface rupturing in historical earthquakes (e.g. Roberts 1996, Galli et al. 2008), they interpreted the presence of at least two palaeoearthquakes. Up to four stripes were noted by Giaccio et al. (2002), but only the two lowest can be correlated along strike for a significant distance. The throws that we have interpreted for these two palaeoearthquakes from examination of the data in Giaccio et al. (2002) and from our own field observations are shown in Figure 7f and g. Both the lowest (youngest) and penultimate event show increases in throw along strike towards the fault tip, coincident with the position of the prominent bend in the fault trace. The cumulative throw produced by both earthquakes shows a clear increase from 0.66 ±0.1 m to 1.0 ±0.1m along strike towards the fault tip. Thus, both the cumulative throw that has accumulated over 15 kyrs, and the throw associated with two palaeoearthquakes over an unknown, but presumably shorter time period depart from the pattern of gradual decrease towards the fault tip in the vicinity of the prominent bend in the fault trace.

Discussion

Our main finding is that an anomaly in the orientation of the Campo Felice fault plane (a change in fault strike around a bend in the fault in this case) has produced an anomaly in vertical motion across the fault, even though the strain-rate represented by the faulting shows a simple, almost linear decrease towards the fault tip. This pattern can be recognised over the timescale of faulting since the last glacial maximum (15 ±3 kyrs) and over the timescale of two palaeoearthquakes (much less than 15 kyrs). These results are similar to those of Faure Walker et al. (2009) who in addition to variations in fault strike, also found that for the Parasano fault, the dip of faults that breach former relay zones also contribute to anomalies in vertical offset, despite a simple, almost linear decrease in strain-rate towards the fault tip. The local anomaly in throw-rates recorded on the Campo Felice fault in this study where the measured value is elevated by ~0.2 mm/yr relative to the value expected given a linear extrapolation of the value towards the fault tip is ~40% of the total variation in throw-rate we have recorded on the studied portion of the fault (range is 0.95-0.45 mm/yr; thus 0.5 mm/yr), representing an anomaly in the linear extrapolated slip of ~33% extra slip. A similar pattern of increased throw-rate was recorded by Faure Walker et al. (2009) who found that the throw-rate doubled along part of the fault where the obliquity of the fault strike relative to the slip-vector increased by ~30^{o} and the fault dip increased by ~6^{o}. Thus, we conclude that relatively small variations in fault orientation measured at the surface can have significant effects on the vertical motions associated with the surface slip distribution.

This leads to the question of what effect variations in fault orientation have on slip at depth. Prominent features of the deformation associated with the 2009 Mw 6.3 L'Aquila earthquake (Fig. 1), are that (1) maxima in surface subsidence and modelled sub-surface slip distributions are skewed towards the southeastern end of the mapped surface rupture, and (2) a 1-2 km-across relay-zone exists between two portions of the surface rupture, and this relay-zone is also located in the southeastern part of the overall rupture trace. All five studies of sub-surface slip distribution illustrated in Figure 1 have chosen to model the deformation with a single fault at depth. If this single fault at depth is to link to the faults at the surface, a significant bend of the fault surface must exist in the sub-surface with an along strike extent of ~4 km and an across strike amplitude of ~2 km. This bend is significantly larger than the example we have measured on the Campo Felice Fault (~0.6 km by ~0.4 km) and also larger than the example on the Parasano Fault described by Faure Walker et al. (2009) (~1 km by ~0.8 km). We suggest that it is likely that this 4 x 2 km bend in the sub-surface fault trace will have affected the magnitude of slip on the fault plane in the 2009 earthquake to produce an anomalous patch of relatively-high vertical motion (subsidence), where the vertical motion could have been tens of percent extra compared to what would have been produced if the fault plane had been planar. The implications of this are as follows:

1) Modelled sub-surface slip distributions are simplifications of the actual slip. The modelled slip distributions shown in Figure 1 are useful in that they allow visualisation of the relationship between surface deformation and slip at depth. However, in detail it is clear that if deviations from planarity of a ruptured fault are not considered the modelled slip distribution is a simplification of the actual slip on the fault.

2) The relationship between slip at the surface, slip at depth and earthquake magnitude will be affected by non-planarity of the fault and the resultant simplification of the modelled slip. The seismic moment of an earthquake is calculated by combining values for the dimensions of the rupture, the stiffness of the ruptured material and the amount of slip (Kostrov 1974). If the amount of slip increases locally due to non-planarity of the fault plane, the derived value for seismic moment will be affected. At present, this process is not considered when relating data on the ruptured fault to seismic moment. This process was also not considered when relating the lengths of ruptures to slip at the surface and slip at depth for databases of historical earthquakes (Wells and Coppersmith 1994), yet this database is used to estimate seismic moment, surface and sub-surface rupture length from slip recorded for palaeoearthquakes described from trenching studies. In summary, if deviations from planarity of a ruptured fault are not considered, this will introduce error into estimation of the seismic moment, slip at depth, surface rupture length and sub-surface rupture length for a single earthquake like the 2009 L'Aquila event; furthermore, this is likely to be one of the reasons for scatter in the relationships between these variables in the database of Wells and Coppersmith (1994) for multiple earthquakes.

3) Stress transfer modelling depends on using the slip distribution from an earthquake to model the stress transfer to so-called "receiver faults" (e.g. Walters et al. 2009). If the modelled slip distribution is a simplification, the stress transfer will also be a simplification. If the modelled slip distribution on a planar fault has concentrations of high slip, that are an artefact of inverting measured anomalies in vertical motion at the surface with a simple planar fault, when in fact the fault in not a single plane, modelled concentrations of high stress will in turn be artefacts – yet it is

these modelled concentrations of high stress on receiver faults that may cause concern in terms of the possibility of imminent triggered slip in a triggered earthquake.

4) Palaeoseismological studies of past earthquakes commonly measure the throw per event throw-rate associated with past events (Galli et al. 2008), but rarely record the spatial variation in fault orientation around the site, usually because the fault plane is poorly-exposed in the unconsolidated material exposed in trenches. However, the fault orientation is essential information if the significance of the throw per event and throw-rate values are to be fully understood. Throw-rates and throw per event measured locally in trenches may typify that portion of the fault if the fault orientation is relatively constant along strike, but conversely, the throw-rate and throw per event may be anomalous if the local fault orientation is anomalous. As throw per event is used to reconstruct likely rupture dimensions and maximum earthquake magnitudes for seismic hazard and engineering design purposes, care must be taken not to forget the spatial continuity of throw per event and hence uncertainty introduced by local changes in fault orientation.

The implications listed above are profound for our understanding of the earthquake process, yet to date we only have two examples where the anomalous slip produced by bends in a fault plane have been quantified (this study and Faure Walker et al. 2009). We suggest that more studies of the geomorphology and structural geology of active faults are needed to produce an empirical relationship between the dimensions of bends in fault planes and the amplitude of vertical deformation.

Conclusions

A study of the structural geology and geomorphology of the well-exposed Campo Felice active normal fault shows that despite a simple linear decrease in strain-rate along strike towards to the fault tip, a change in fault strike has produced a localised anomaly in vertical motion, with the throw-rate increasing by ~40% close to the fault bend. The throw anomaly can be resolved both over a timescale of multiple seismic cycles (15 ±3 ka in this case) or over the timescale of two individual palaeoearthquakes (<15 kyrs). This example is well explained by theoretical considerations advanced by Faure Walker et al. (2009), who show that horizontal strain-rates and rates of vertical and horizontal deformation are linked by variables that include fault slip vectors and fault orientations. A 4 x 2 km across relay zone in the surface ruptures to the 2009 L'Aquila earthquake (Mw 6.3) on the neighbouring Paganica fault is likely to be underlain by a bend in the fault trace at depth of similar dimensions. The theory of Faure Walker et al. (2009) suggests that a bend of this size will produce a significant local anomaly in throw per event and throw-rate on the fault. An anomaly in surface deformation recorded by InSAR for the earthquake does exist, as surface subsidence is skewed towards the southeastern end of the rupture trace, with a maxima in the vicinity of the aforementioned relay zone. Early attempts to model this deformation have used a planar fault, but we suggest that improved sub-surface slip distributions will be achieved if a non-planar fault with a change in strike is utilised. Surface and sub-surface slip distributions are used to model stress transfer and calculate maximum magnitudes for palaeoearthquakes. We suggest the orientation of the fault plane in question should be considered with care as uncertainty in fault plane orientation relative to the slip-vector will produce uncertainty in derived stress transfer and maximum magnitude estimates. Studies of the geomorphology are a key input for the construction of a database documenting the effects of such fault bends will be that is offset around active faults.

Acknowledgements

This work was funded by NERC Grants NE/H003266/1, NE/E01545X/1, NE/B504165/1, GR9/02995 and NE/I024127/1, a studentship to J.P. Faure Walker (NER/S/A/2006/14042) and the Doctoral Fellowship scheme at Durham University.

References

Atzori, S., Hunstad,I., Chini,M., Salvi, S., Tolomei, C., Bignami, C., Stramondo, S., Trasatti, E., Antonioli, A., Boschi, E., Finite fault inversion of DInSAR coseismic displacement of the 2009 L'Aquila earthquake (central Italy). Geophysical Research Letters,VOL.36, L15305, doi:10.1029/2009GL039293, 2009.

Boncio, P., Pizzi, A., Brozzetti, G., Pomposo, G., Lavecchia, G., Di Naccio, D., Ferrarini, F., Coseismic ground deformation of the 6 April 2009 L'Aquila earthquake (central Italy, Mw6.3)., Geophysical Research Letters, Vol. 37, L06308, doi:10.1029/2010GL042807, 2010.

Cheloni,D.,et al. (2010), Coseismic and initial post-seismic slip of the 2009 Mw6.3 L'Aquila earthquake, Italy, from GPS measurements, Geo-phys. J.I nt.,181, 1539–1546,doi:10.1111/j.1365-246X.2010.04584.x.

Cirella, A., A. Piatanesi, M. Cocco, E. Tinti, L. Scognamiglio, A. Michelini, A. Lomax, E. Boschi. Rupture history of the 2009 L'Aquila (Italy) earthquake from non-linear joint inversion of strong motion and GPS data. Geophysical Research Letters,VOL.36, L19304, doi:10.1029/2009GL039795, 2009.

Calderoni, G., Di Giovambattista, R., Vannoli, P. Pucillo, S. & Rovelli, A. Fault-trapped waves depict continuity of the fault system responsible for the 6 April 2009 Mw 6.3 L'Aquila earthquake, central Italy. Earth and Planetary Science Letters, 323-324, 1-8.

Crosby, C. J., Krishnan, S., Arrowsmith, J. R., Kim, H. S., Colunga, J., Alex, N., & Baru, B, in review. Points2Grid: An Efficient Local Gridding Method for DEM Generation from Lidar Point Cloud Data. Geosphere special issue on Applications of Lidar in the Earth Sciences.

D'Agostino N., Jackson J., Dramis F., and Funiciello R., Interactions between mantle upwelling, drainage evolution and active normal faulting: an example from the central Apennines (Italy), Geophysical Journal International, 147, 475-497, 2001

D'Agostino,N.,D. Cheloni,G. Fornaro,R. Giuliani,.Reale, D., (2012),Space-time distribution of afterslip following the 2009 L'Aquila earthquake, J. Geophys. Res., 117,B02402,doi:10.1029/2011JB008523.

Delaunay, B., 1934. Sur la sphère vide, Izvestia Akademii Nauk SSSR, Otdelenie Matematicheskikh i Estestvennykh Nauk, 7, 793–800.

Faure Walker, J. P., Roberts, G. P., Cowie, P. A., Papanikolaou, I., Sammonds, P. R., Michetti, A. M. & Phillips, R. J., 2009. Horizontal strain-rates and throw-rates across breached relay zones, central Italy: Implications for the preservations of throw deficits at points of normal fault linkage. J Struct Geol, 31, 1145-1160.

Faure Walker, J. P., Roberts, G. P., Cowie, P. A., Papanikolaou, I., Michetti, A. M., Sammonds, Wilkinson, M., McCaffrey, K. J. W., P., Phillips, R., Relationship between topography and strain-rate in the actively-extending Italian Apennines. Earth and Planetary Science Letters, Volumes 325–326, 1 April 2012, Pages 76–84. doi.org/10.1016/j.epsl.2012.01.028. 2012.

Faure Walker, J. P., Roberts, G. P., Sammonds, P., Cowie, P. A., Comparison of earthquakes strains over 10^2 and 10^4 year timescales: insights into variability in the seismic cycle in the central Apennines, Italy. Journal of Geophysical Research, VOL.115, B10418, doi:10.1029/2009JB006462, 2010.

Giaccio, B. ,F.Galadini, A. Sposato, P. Messina, M. Moro, M. Zreda, A. Cittadini ,S. Salvi, A. Todero. Image processing and roughness analysis of exposed bedrock fault planes as a tool for paleoseismological analysis: results from the Campo Felice fault (central Apennines, Italy). Geomorphology, 49, 281-301, 2002.

Galadini F. and Galli P., Active Tectonics in the Central Apennines (Italy) - Input Data for Seismic Hazard Assessment, Natural Hazards, 22, 225-270, 2000

Galli, P., Galadini, F., Pantosti, D., Twenty years of paleoseismology in Italy. Earth Science Reviews, 88, 89-117, 2008.

Kostrov V.V., Seismic Moment and Energy of Earthquakes, and Seismic Flow of Rock, Izv., Earth Physics,1, 23-40, 1974, (translation UDC 550.341, 13-21)

Michetti A.M., Brunamonte F., Serva L., Vittori E., Trench investigations of the 1915 Fucino earthquake fault scarps (Abruzzo, Central Italy): geological evidence of large historical events, Journal of Geophysical Research, 101 (B3), 5921-5936, 1996

Pace B., Peruzza L., Lavecchia G., and Boncio P., Global seismogenic source modelling and probabilistic seismic hazard analysis in Central Italy, Bulletin of the Seismological Society of America, 96 (1), 107–132, 2006

Papanikolaou, I. D., Foumelis, M., Paracharidis, E. L., Lekkas, J., and Fountoulis, G., Deformation pattern of the 6 and 7 Aoril 2009, M = 6.3 and Mw 5.6 earthquakes in L'Aquila (central Italy) revealed by ground and space observations, Nat. Hazards, Earth Syst. Sci. 10, 73-87, 2010.

Roberts G.P. and Michetti A.M., Spatial and temporal variations in growth rates along active normal fault systems: an example from the Lazio-Abruzzo Apennines, central Italy, Journal of Structural Geology, 26, 339-376, 2004

Roberts, G. P. 1996. Noncharacteristic earthquake ruptures from the Gulf of Corinth, Greece. Journal of Geophysical Research, 101, 25,255-25,267.

Roberts, G. P., Raithatha, B., Sileo, G, Pizzi, A., Pucci, S., Faure Walker, J., Wilkinson, M., McCaffrey, K., Phillips, R. J., Michetti, A. M., Guerrieri, L., Blumetti, A. M., Vittori, E., Cowie, P. A., Sammonds, P., Galli, P., Boncio, P., Bristow, C., Walters, R., Shallow sub-surface structure of the 6th April 2009 Mw 6.3 L'Aquila earthquake surface rupture at Paganica, investigated with Ground Penetrating Radar. Geophysical Journal International. Doi:10.1111/j.1365-246X.2010.04713.x. 2010.

Vezzani, L., Ghisetti, F., Carta Geologica Dell'Abruzzo, 1:100000, SELCA, Via R. Giuliani, 153 – Firenze, 1998.

Walters, R. J., J. R. Elliott, N. D'Agostino, P. C. England, I. Hunstad, J. A. Jackson, B. Parsons, R. J. Phillips, and G. P. Roberts. The 2009 L'Aquila earthquake (central Italy): A source mechanism and implications for seismic hazard, Geophys. Res. Lett., 36, L17312, doi:10.1029/2009GL039337. 2009.

Wells, D. L., & Coppersmith, K. J., 1994. New empirical relationships among magnitude, rupture length, rupture width, rupture area and surface displacement, Bull. Seismol. Soc. Am., 84, 974–1002.

Figure Captions

Figure 1 Map of surface deformation and modelled sub-surface slip distributions for the 2009 Mw 6.3 L' Aquila earthquake, Italy. (a) Surface ruptures adapted from Boncio et al. (2010) with contours of "coseismic" surface displacements recorded by InSAR between 4th April 2009 and 12th April 2009 adapted from D'Agostino et al. (2012). dashed line approximates the modelled planar, rectangular faults in panels b-f. (b)-(f) Range of modelled slip distributions from different combinations of InSAR, GPS and strong motion data. Red lines on b-f show the extent of surface faulting from Boncio et al. (2010). Note the relative positions of the maxima for surface deformation and sub-surface slip distributions; the maxima are skewed towards the SE tip of the surface ruptures.

Figure 2 Location map for active faults in central Italy on a 20 m DEM. Boxes locate Figs. 1 and 3.

Figure 3 Location maps for the Campo Felice. (a) Geological map adapted from Giaccio et al. (2002) and Vezzani and Ghisetti 1998. (b) Aerial photograph from Google Earth™. The faults offset Cretaceous carbonates with normal sense displacements, controlling the position of a Quaternary Holocene intra-montane basin, and have offset a former (Quaternary?) drainage course.

Figure 4. LiDAR data, processing and analysis. (a) Point cloud data. (b) Manual removal of vegetation from point cloud. (c) Contour map. (d) TIN surface with the locations of 25 study sites where 10 scarp profiles were produced (250 scarp profiles in total). Each red line is actually 10 profile lines spaced 1m apart along strike. A representative set of 25 scarp profiles from the 25 locations indicated are shown in Figure 5. (e) A surface dip map using the dip calculation algorithm in goCAD and displayed in Google Earth. Blue colours correspond to low values of dip ~ 20 degrees. Yellow colours correspond to moderate values of dip ~ 40 degrees. Red colours correspond to high values of dip ~ 60 degrees.

Figure 5 Scarp profiles derived from terrestrial laser scan data (TLS) from the 25 sites indicated in Figure 4d, showing offsets of a 15 ± 3 ka periglacial slope. These 25 profiles are a sub-set of the 250 profiles generated to produce the values and error bars in Figure 7. Offsets were studied using *Crossint*.

Figure 6 Lower hemisphere stereographic projection of the orientation of fault planes and the slip-vector orientation defined by striated faults, showing how the kinematics of faulting vary along the Campo Felice fault. Data were collected from the 25 locations shown in Figure 4, but have been grouped together to form this figure.

Figure 7 Graphs showing the relationship between fault orientation and rates of faulting for the Campo Felice fault. (a) Fault strike. Error bars are $\pm 3^{o}$. The red line is a moving point average of five measurements. (b) Fault dip. Error bars are $\pm 3^{o}$. The red line is a moving point average of five measurements. (c) Slip vector azimuth. Error bars are $\pm 3^{o}$. The red line is a moving point average of five measurements. (d) Post 15 ± 3 ka throw measured with TLS. (e) Throw and principle horizontal strain-rate (see Table 1). Strain-rate was calculated in 250 x 250 m boxes using the equations in the text. The error bars for throw are $\pm 1\ \sigma$ for measurements of throw alone, not including those for uncertainty in age, whilst those for strain-rate are $\pm 2\sigma$. A throw-rate scale is also shown on the y axis for 3 scenarios for the age of the offset slope (12 ka, 15 ka and 18 ka) – our preferred estimate of the age is 15 ± 3 as it encompasses our assessment of the uncertainty (see Faure Walker et al. 2010 for discussion). (f) and (g) vertical offsets associated with two palaeoearthquakes recorded by stripes of freshly-exposed fault plane at the base of the exposed fault plane reported by Giaccio et al. (2002), but modified slightly during our own fieldwork. Errors on field estimates of the throw for these palaeoearthquakes are estimated to be ± 0.1 m.

Figure 8 Summary cartoon showing how the location of maximum coseismic subsidence associated with the 2009 L'Aquila Earthquake (Ms 6.3) may relate to the sub-surface geometry of the fault. We speculate that the segmented fault at surface coalesces into a single curved fault at depth, and the along-strike bend in the fault requires high values for vertical motion following the relationships quantified by Faure Walker et al. (2009).

Table 1 Data used to calculate strain-rate in 250 m bins along strike

Plunge of kinematic slip (degrees from horizontal)	Strike of fault (degrees from north)	Kinematic slip direction (degrees from north)	Throw (m)	Distance along strike (m)	Strain-rate (ppm/yr)
47	128	213	13.77	125	3.41
47	129	213	14.19	375	3.52
47	134	208	12.63	625	3.08
52	136	208	12.74	875	2.59
50	135	210	10.98	1125	2.42
52	138	213	11.02	1375	2.25
51	134	212	9.62	1625	2.05
53	118	215	10.05	1875	1.99
54	104	210	10.55	2125	1.86
55	105	209	11.19	2375	1.91
53	113	209	10.87	2625	2.09
53	142	208	9.47	3375	1.82
54	148	221	8.80	3625	1.60
55	153	222	8.31	3875	1.39
55	153	249	7.30	4375	1.04

Figure 1

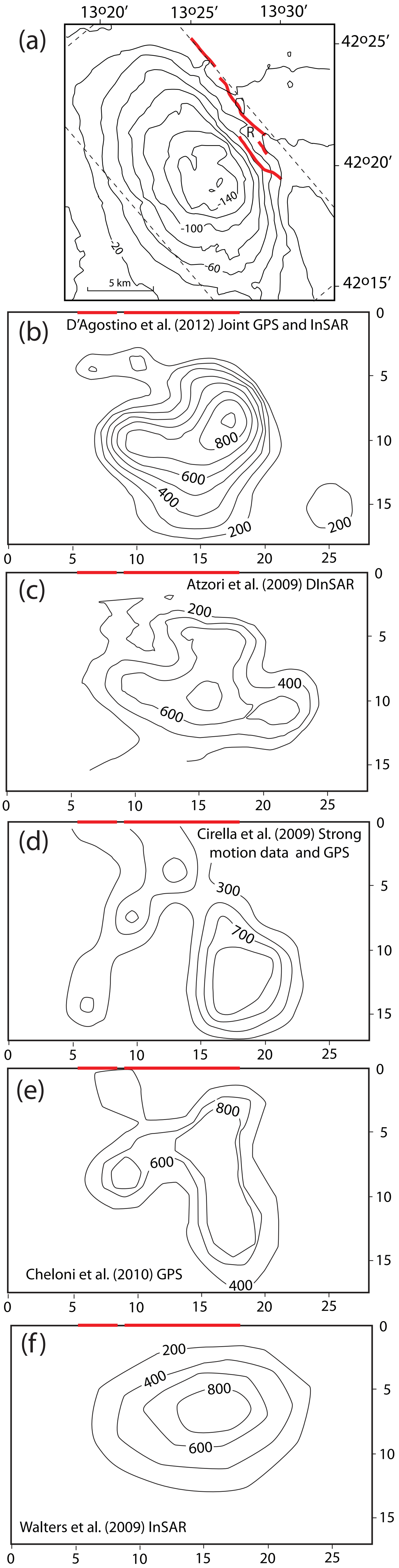

(a)
13°20′
13°25′
13°30′
42°25′
42°20′
42°15′
R
-140
-100
-60
20
5 km
(b)
D'Agostino et al. (2012) Joint GPS and InSAR
800
600
400
200
200
(c)
Atzori et al. (2009) DInSAR
200
400
600
(d)
Cirella et al. (2009) Strong motion data and GPS
300
700
(e)
800
600
400
Cheloni et al. (2010) GPS
(f)
200
400
800
600
Walters et al. (2009) InSAR
0
5
10
15
20
25

Figure 2

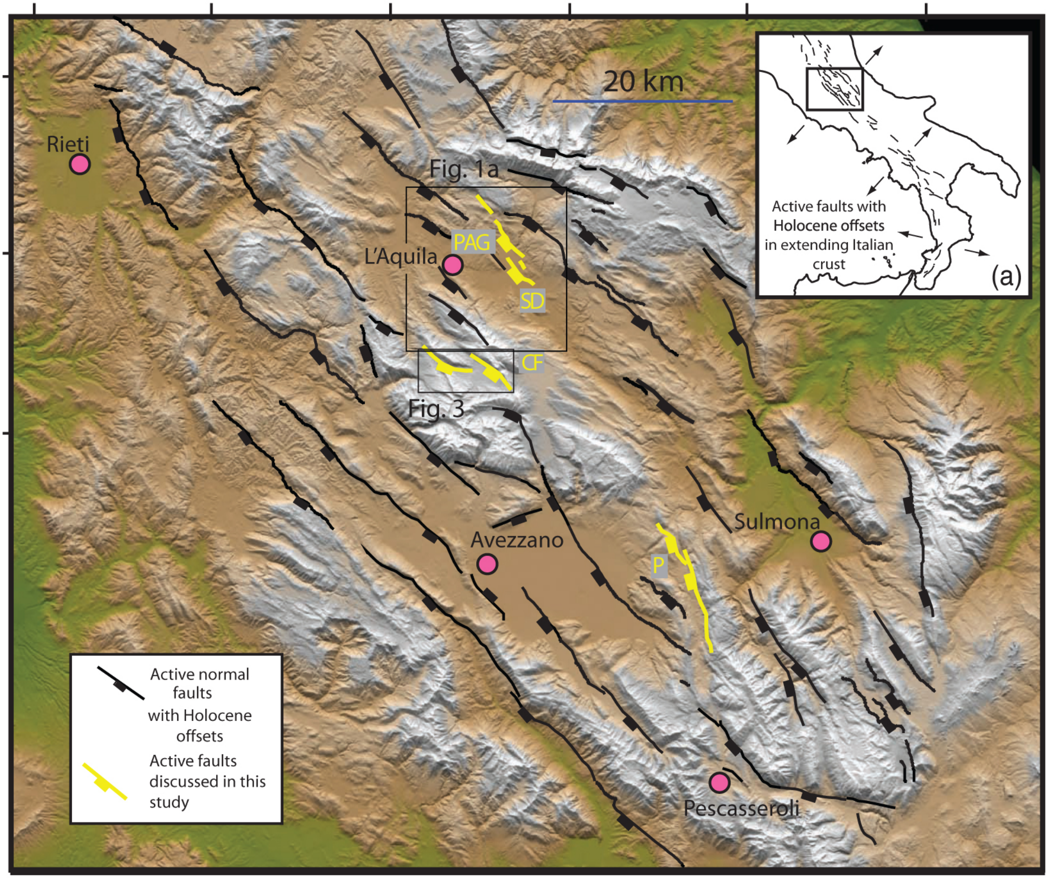

20 km
Rieti
Fig. 1a
PAG
L'Aquila
SD
CF
Fig. 3
Avezzano
Sulmona
P
Pescasseroli
Active faults with Holocene offsets in extending Italian crust
(a)
Active normal faults with Holocene offsets
Active faults discussed in this study

Figure 3

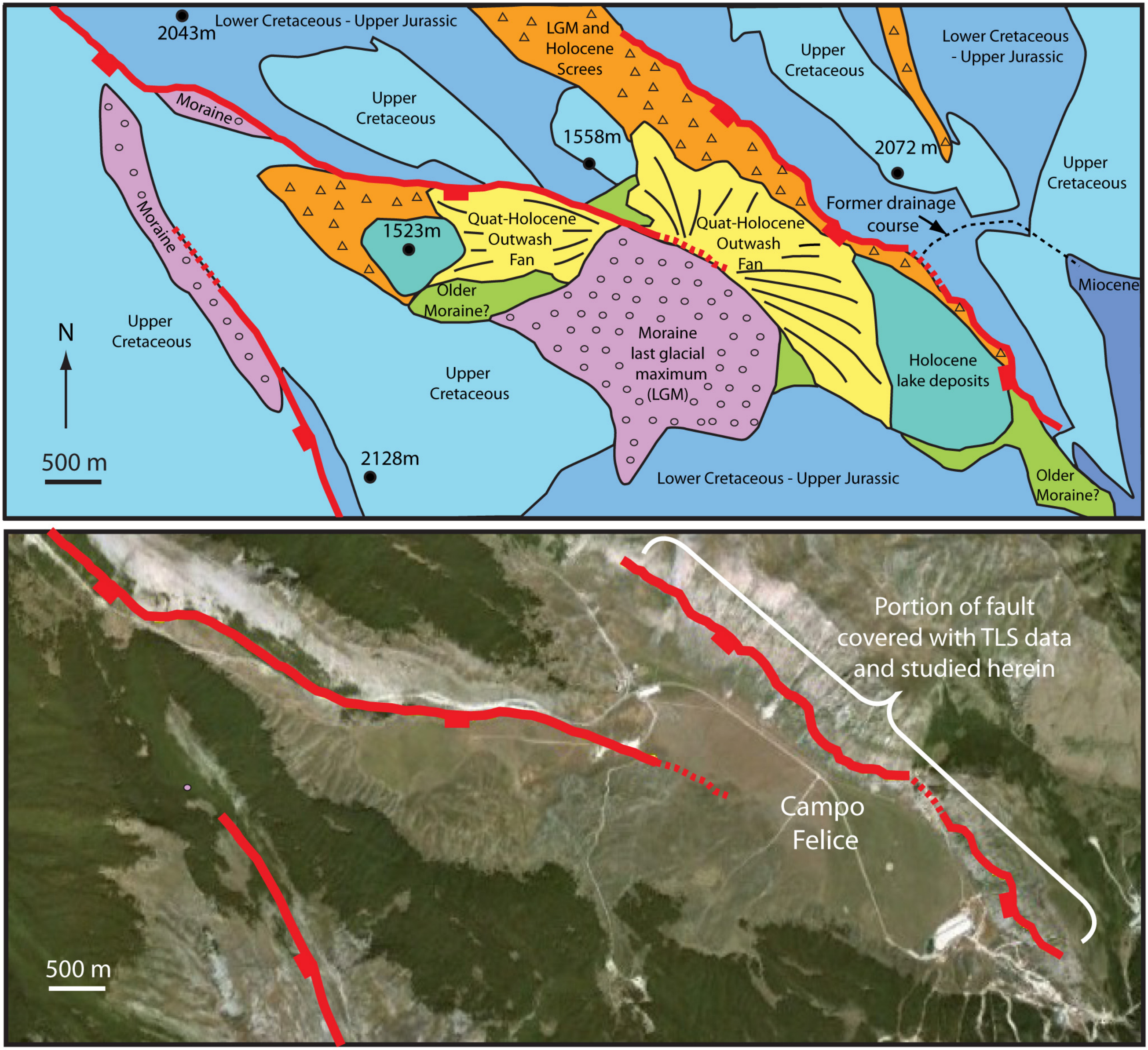
Lower Cretaceous - Upper Jurassic
2043m
LGM and Holocene Screes
Upper Cretaceous
Lower Cretaceous - Upper Jurassic
Moraine
Upper Cretaceous
1558m
2072 m
Upper Cretaceous
Former drainage course
Moraine
1523m
Quat-Holocene Outwash Fan
Quat-Holocene Outwash Fan
Miocene
Older Moraine?
N
Upper Cretaceous
Moraine last glacial maximum (LGM)
Holocene lake deposits
Upper Cretaceous
500 m
2128m
Lower Cretaceous - Upper Jurassic
Older Moraine?
Portion of fault covered with TLS data and studied herein
Campo Felice
500 m

Figure 4

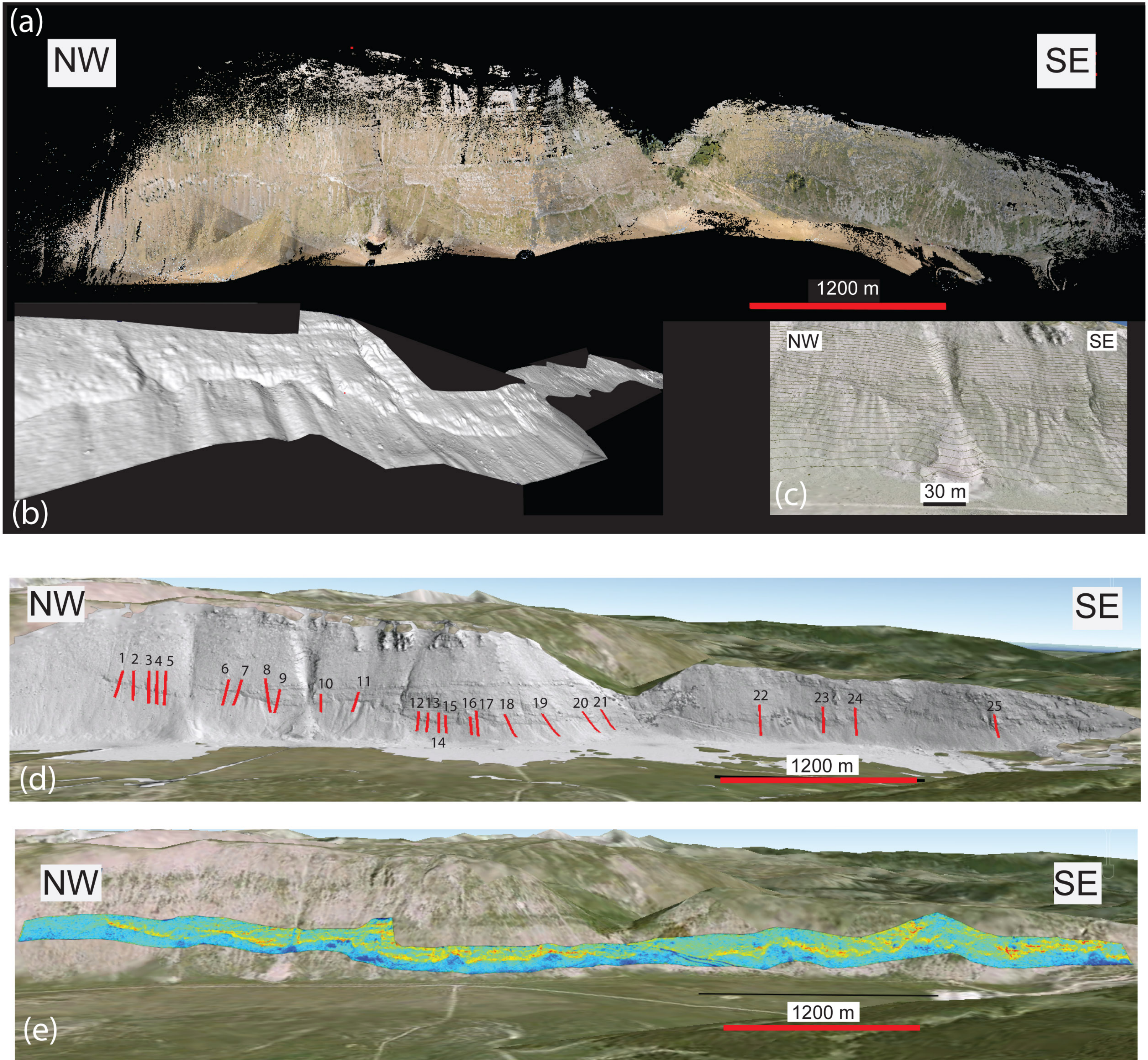
(a)
NW
SE
1200 m
(b)
NW
SE
30 m
(c)
NW
SE
1 2 3 4 5
6 7 8 9
10
11
12 13 15 16 17 18
14
19
20 21
22
23
24
25
1200 m
(d)
NW
SE
1200 m
(e)

Figure 5

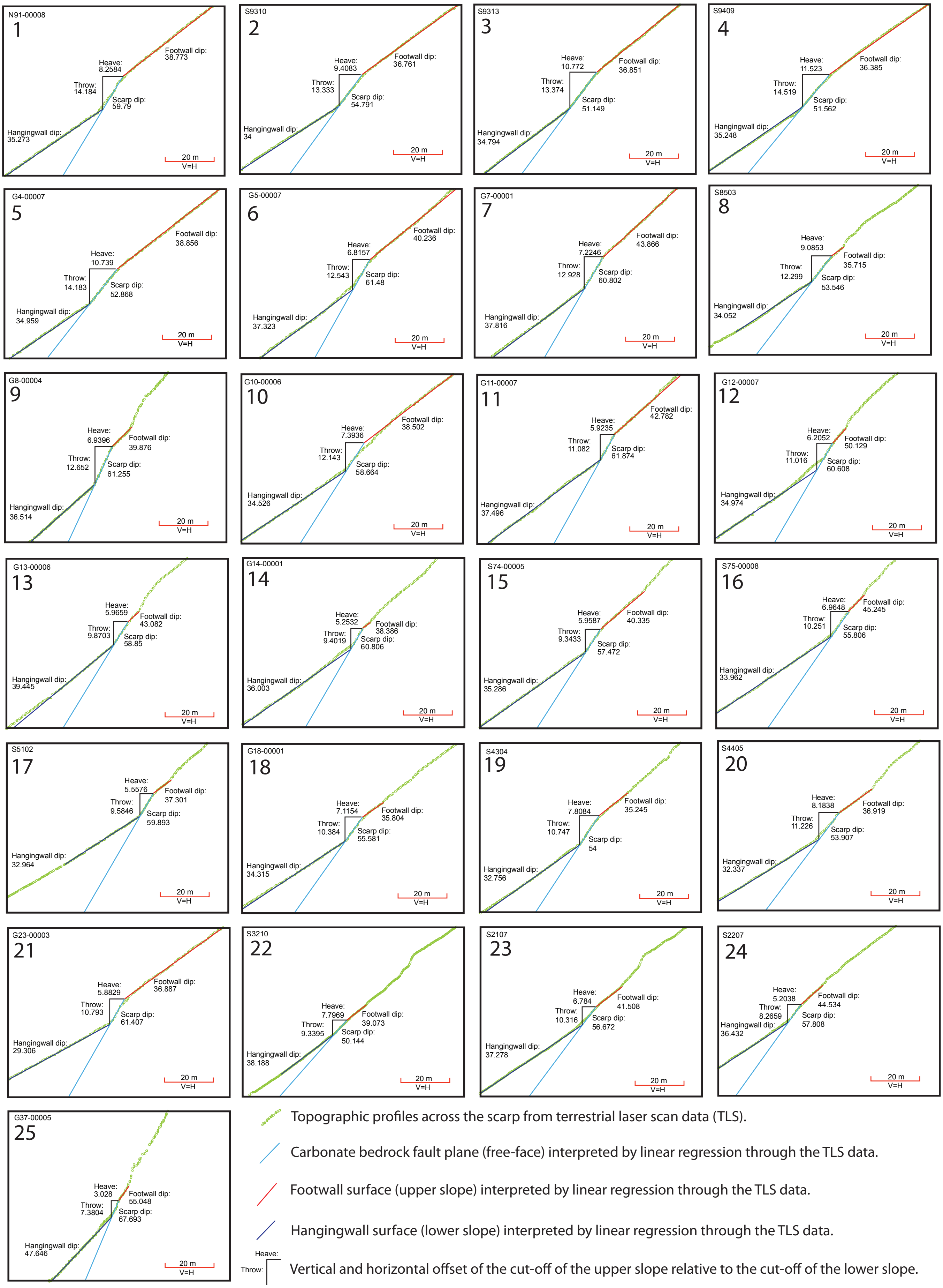
N91-00008
1
Heave: 8.2584
Throw: 14.184
Footwall dip: 38.773
Scarp dip: 59.79
Hangingwall dip: 35.273
20 m
V=H
S9310
2
Heave: 9.4083
Throw: 13.333
Footwall dip: 36.761
Scarp dip: 54.791
Hangingwall dip: 34
20 m
V=H
S9313
3
Heave: 10.772
Throw: 13.374
Footwall dip: 36.851
Scarp dip: 51.149
Hangingwall dip: 34.794
20 m
V=H
S9409
4
Heave: 11.523
Throw: 14.519
Footwall dip: 36.385
Scarp dip: 51.562
Hangingwall dip: 35.248
20 m
V=H
G4-00007
5
Heave: 10.739
Throw: 14.183
Footwall dip: 38.856
Scarp dip: 52.868
Hangingwall dip: 34.959
20 m
V=H
G5-00007
6
Heave: 6.8157
Throw: 12.543
Footwall dip: 40.236
Scarp dip: 61.48
Hangingwall dip: 37.323
20 m
V=H
G7-00001
7
Heave: 7.2246
Throw: 12.928
Footwall dip: 43.866
Scarp dip: 60.802
Hangingwall dip: 37.816
20 m
V=H
S8503
8
Heave: 9.0853
Throw: 12.299
Footwall dip: 35.715
Scarp dip: 53.546
Hangingwall dip: 34.052
20 m
V=H
G8-00004
9
Heave: 6.9396
Throw: 12.652
Footwall dip: 39.876
Scarp dip: 61.255
Hangingwall dip: 36.514
20 m
V=H
G10-00006
10
Heave: 7.3936
Throw: 12.143
Footwall dip: 38.502
Scarp dip: 58.664
Hangingwall dip: 34.526
20 m
V=H
G11-00007
11
Heave: 5.9235
Throw: 11.082
Footwall dip: 42.782
Scarp dip: 61.874
Hangingwall dip: 37.496
20 m
V=H
G12-00007
12
Heave: 6.2052
Throw: 11.016
Footwall dip: 50.129
Scarp dip: 60.608
Hangingwall dip: 34.974
20 m
V=H
G13-00006
13
Heave: 5.9659
Throw: 9.8703
Footwall dip: 43.082
Scarp dip: 58.85
Hangingwall dip: 39.445
20 m
V=H
G14-00001
14
Heave: 5.2532
Throw: 9.4019
Footwall dip: 38.386
Scarp dip: 60.806
Hangingwall dip: 36.003
20 m
V=H
S74-00005
15
Heave: 5.9587
Throw: 9.3433
Footwall dip: 40.335
Scarp dip: 57.472
Hangingwall dip: 35.286
20 m
V=H
S75-00008
16
Heave: 6.9648
Throw: 10.251
Footwall dip: 45.245
Scarp dip: 55.806
Hangingwall dip: 33.962
20 m
V=H
S5102
17
Heave: 5.5576
Throw: 9.5846
Footwall dip: 37.301
Scarp dip: 59.893
Hangingwall dip: 32.964
20 m
V=H
G18-00001
18
Heave: 7.1154
Throw: 10.384
Footwall dip: 35.804
Scarp dip: 55.581
Hangingwall dip: 34.315
20 m
V=H
S4304
19
Heave: 7.8084
Throw: 10.747
Footwall dip: 35.245
Scarp dip: 54
Hangingwall dip: 32.756
20 m
V=H
S4405
20
Heave: 8.1838
Throw: 11.226
Footwall dip: 36.919
Scarp dip: 53.907
Hangingwall dip: 32.337
20 m
V=H
G23-00003
21
Heave: 5.8829
Throw: 10.793
Footwall dip: 36.887
Scarp dip: 61.407
Hangingwall dip: 29.306
20 m
V=H
S3210
22
Heave: 7.7969
Throw: 9.3395
Footwall dip: 39.073
Scarp dip: 50.144
Hangingwall dip: 38.188
20 m
V=H
S2107
23
Heave: 6.784
Throw: 10.316
Footwall dip: 41.508
Scarp dip: 56.672
Hangingwall dip: 37.278
20 m
V=H
S2207
24
Heave: 5.2038
Throw: 8.2659
Footwall dip: 44.534
Scarp dip: 57.808
Hangingwall dip: 36.432
20 m
V=H
G37-00005
25
Heave: 3.028
Throw: 7.3804
Footwall dip: 55.048
Scarp dip: 67.693
Hangingwall dip: 47.646
20 m
V=H
Topographic profiles across the scarp from terrestrial laser scan data (TLS).
Carbonate bedrock fault plane (free-face) interpreted by linear regression through the TLS data.
Footwall surface (upper slope) interpreted by linear regression through the TLS data.
Hangingwall surface (lower slope) interpreted by linear regression through the TLS data.
Heave:
Throw:
Vertical and horizontal offset of the cut-off of the upper slope relative to the cut-off of the lower slope.

Figure 6

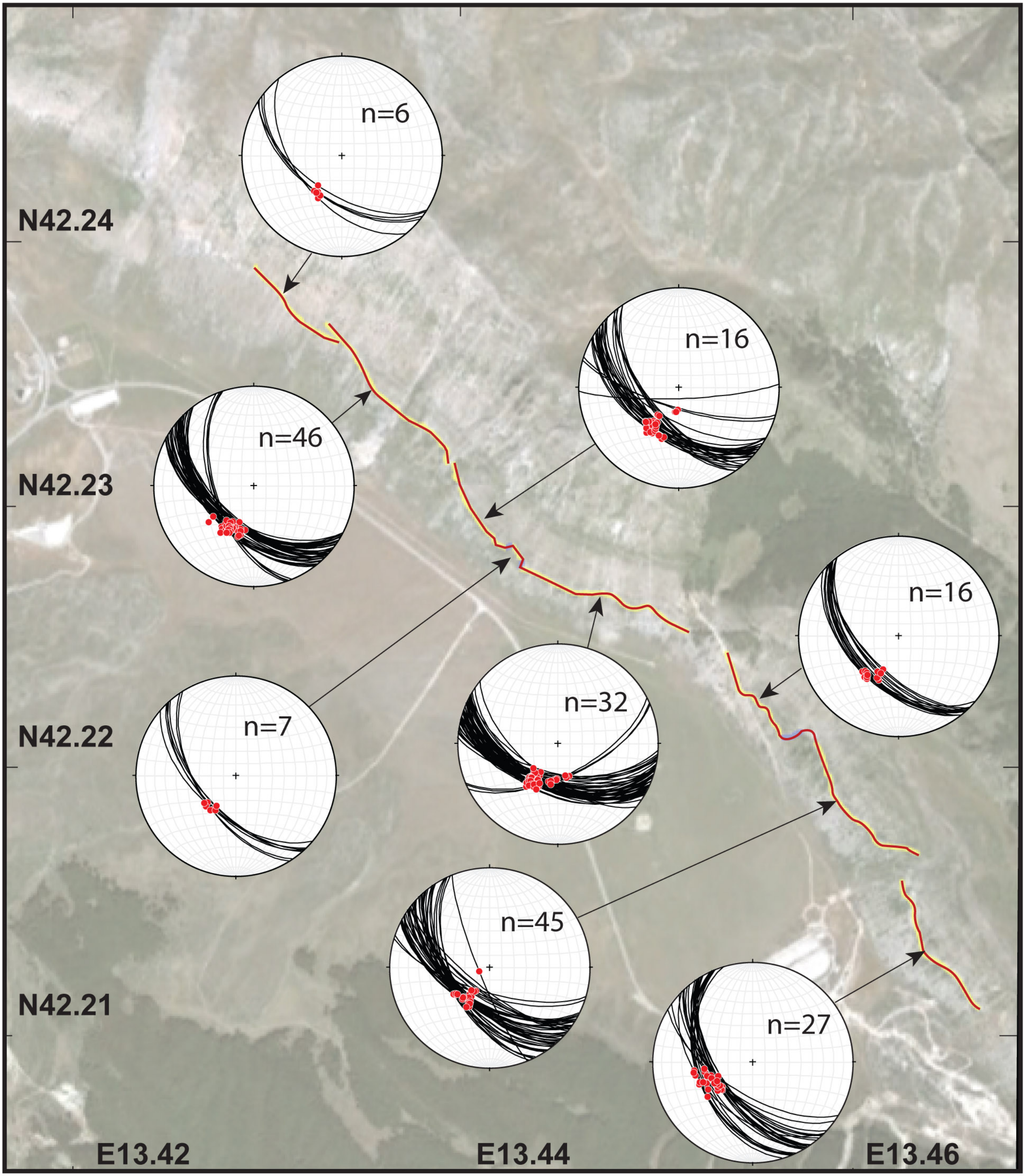

N42.24
N42.23
N42.22
N42.21
E13.42
E13.44
E13.46
n=6
n=46
n=16
n=16
n=7
n=32
n=45
n=27

Figure 7

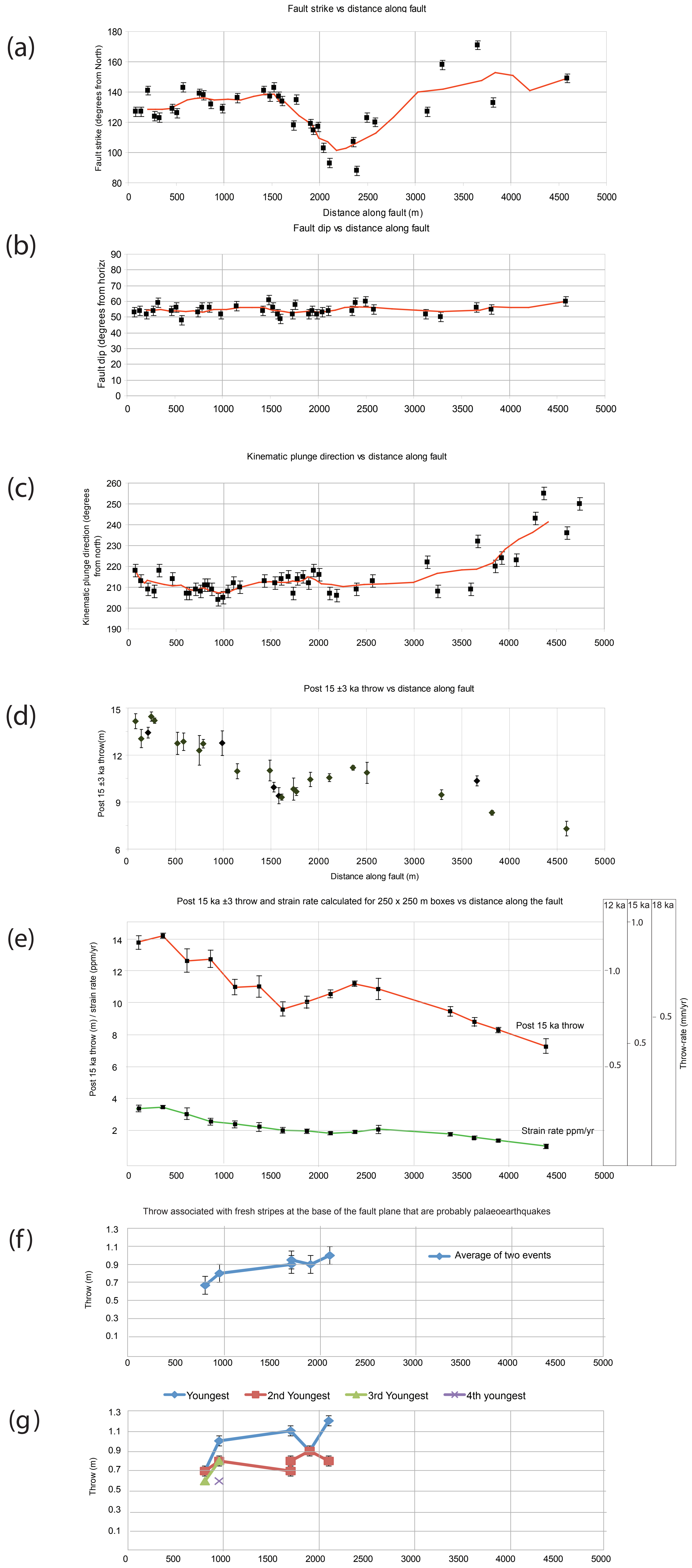
(a)
Fault strike vs distance along fault
Fault strike (degrees from North)
Distance along fault (m)
(b)
Fault dip vs distance along fault
Fault dip (degrees from horizo
(c)
Kinematic plunge direction vs distance along fault
Kinematic plunge direction (degrees from north)
(d)
Post 15 ±3 ka throw vs distance along fault
Post 15 ±3 ka throw(m)
Distance along fault (m)
(e)
Post 15 ka ±3 throw and strain rate calculated for 250 x 250 m boxes vs distance along the fault
Post 15 ka throw (m) / strain rate (ppm/yr)
12 ka
15 ka
18 ka
Throw-rate (mm/yr)
Post 15 ka throw
Strain rate ppm/yr
(f)
Throw associated with fresh stripes at the base of the fault plane that are probably palaeoearthquakes
Throw (m)
Average of two events
(g)
Youngest
2nd Youngest
3rd Youngest
4th youngest
Throw (m)

Figure 8

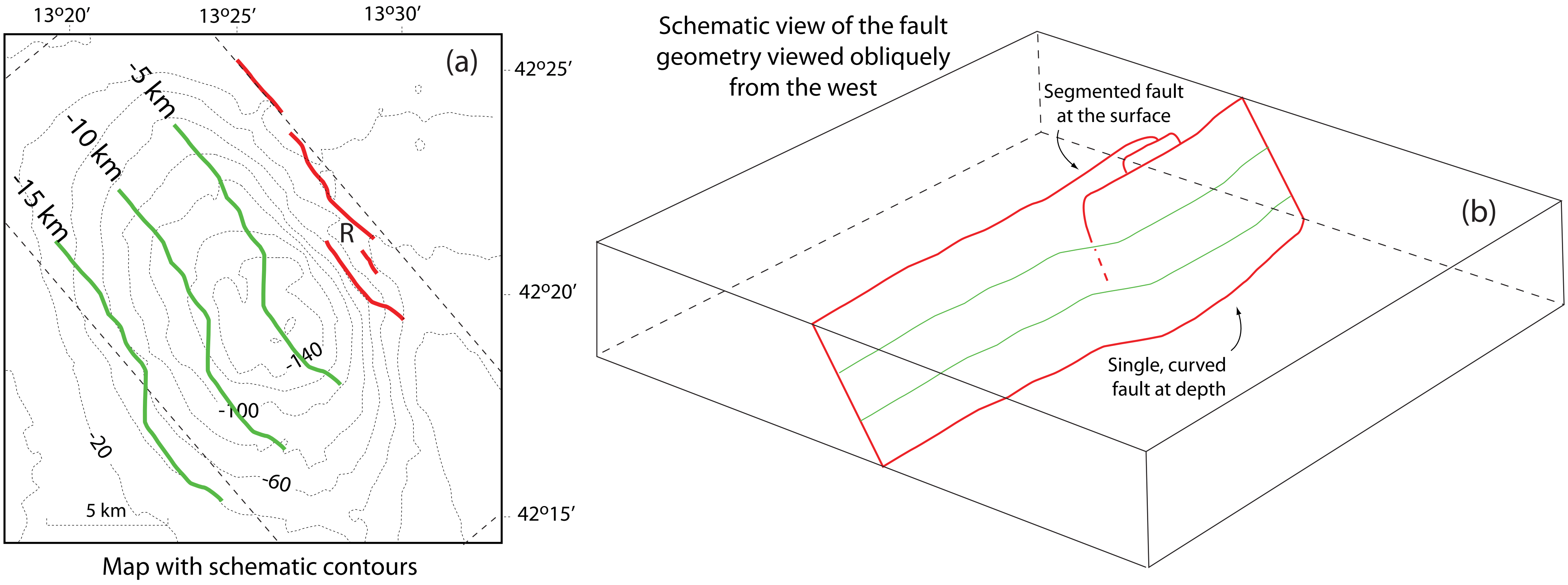

Map with schematic contours drawn on the fault plane at depth